

## ARTICLE OPEN



# Valley-filling instability and critical magnetic field for interaction-enhanced Zeeman response in doped WSe<sub>2</sub> monolayers

Fengyuan Xuan<sup>1</sup> and Su Ying Quek<sup>1,2,3,4</sup>✉

Carrier-doped transition metal dichalcogenide (TMD) monolayers are of great interest in valleytronics due to the large Zeeman response (g-factors) in these spin-valley-locked materials, arising from many-body interactions. We develop an ab initio approach based on many-body perturbation theory to compute the interaction-enhanced g-factors in carrier-doped materials. We show that the g-factors of doped WSe<sub>2</sub> monolayers are enhanced by screened-exchange interactions resulting from magnetic-field-induced changes in band occupancies. Our interaction-enhanced g-factors  $g^*$  agree well with experiment. Unlike traditional valleytronic materials such as silicon, the enhancement in g-factor vanishes beyond a critical magnetic field  $B_c$  achievable in standard laboratories. We identify ranges of  $g^*$  for which this change in g-factor at  $B_c$  leads to a valley-filling instability and Landau level alignment, which is important for the study of quantum phase transitions in doped TMDs. We further demonstrate how to tune the g-factors and optimize the valley-polarization for the valley Hall effect.

npj Computational Materials (2021) 7:198; <https://doi.org/10.1038/s41524-021-00665-8>

## INTRODUCTION

Valleytronics, the control and manipulation of the valley degree of freedom (valley pseudospin), is being actively considered as the next paradigm for information processing. The field of valleytronics dates back to investigations on traditional semiconductors such as silicon<sup>1,2</sup>, but the ability to exploit valley polarization in these materials has been limited<sup>3</sup>. A major impetus for the renaissance of valleytronics is the recent discovery that H-phase transition metal dichalcogenide (TMD) semiconductor monolayers (MLs) are excellent candidates for valleytronics applications<sup>3,4</sup>. The spin-valley locking effect in these MLs<sup>5</sup> leads to long lifetimes for spin- and valley-polarization, while individual valleys can be probed and controlled using circularly-polarized light, paving the way to use the valley pseudospin for information processing. The valley Zeeman response in TMD MLs<sup>6–20</sup> is also significantly larger than in traditional semiconductors<sup>21–27</sup>.

When an external magnetic field is applied normally to the TMD ML, the energies of the valleys shift in equal magnitude and opposite directions. This Zeeman effect is quantified by the orbital and spin magnetic moments, which contribute to the Landé g-factors. In TMD MLs, the intrinsic Landé g-factors are about six times larger<sup>6–8,10</sup> than that in silicon, where only the spin magnetic moment dominates<sup>21,22</sup>. The larger g-factors in TMD MLs allow for greater control in tuning the energetics of the valley pseudospins and results in a larger valley-polarized current, which is important for observations of the valley Hall effect<sup>3</sup>. Besides the Zeeman effect, an external magnetic field also results in a quantization of states to form Landau levels (LLs).

Much of the current research on valleytronics seeks to understand how to manipulate the valley pseudospins in TMDs<sup>3,4</sup>. It has been found that carrier doping can dramatically enhance the g-factors in TMD monolayers<sup>14–20</sup>, opening up the possibility to tune the valley pseudospin by gating in a magnetic field. This

enhancement in g-factors has been attributed to many-body interactions<sup>14–20,23,26</sup>, but a quantitative understanding is lacking. To interpret the g-factor enhancement in doped TMDs, experimentalists have typically relied on existing theoretical literature dating back to the 1960s–1970s<sup>23,28</sup>. However, there are two shortcomings of these theoretical approaches. Firstly, they are not ab initio methods and cannot provide quantitative predictions. Secondly, these studies all focused on silicon or III-V semiconductors, which are very different in nature from the TMD monolayers. It is important to question if the experimental observations on g-factors in doped TMDs serve only to validate in TMDs what was already known for silicon, or if it is possible to observe emergent phenomena not known before in conventional valleytronics materials.

In this work, we develop an ab initio approach based on many-body perturbation theory to compute the interaction-enhanced Landé g-factors in carrier-doped systems. We predict that the larger intrinsic g-factors in TMD MLs enable the observation of a critical magnetic field  $B_c$  above which the interaction-induced enhancement in the g-factors vanishes in doped TMDs. We identify ranges of the enhanced g-factor  $g_{\text{enh}}^*$  for which the discontinuous change in g-factor at  $B_c$  results in a LL alignment and valley-filling instability for  $B \gtrsim B_c$ . Such a phenomenon has not been observed or predicted for silicon and other conventional valleytronic materials. Our computed interaction-enhanced g-factors for hole-doped ML WSe<sub>2</sub> agree well with experiment<sup>14,16,18</sup> and can be tuned by dielectric screening. The predicted valley-filling instability for  $B \gtrsim B_c$  provides theoretical insights into recent experimental observations<sup>16</sup> of a pronounced Landau level-filling instability at a critical magnetic field which closely matches our predicted values. The associated alignment of LLs is of interest<sup>16</sup> to investigate quantum phase transitions in these doped TMDs<sup>29–34</sup>. The recent observation of fractional quantum Hall states associated with non-

<sup>1</sup>Centre for Advanced 2D Materials, National University of Singapore, 6 Science Drive 2, Singapore 117546, Singapore. <sup>2</sup>Department of Physics, National University of Singapore, 2 Science Drive 3, Singapore 117551, Singapore. <sup>3</sup>NUS Graduate School Integrative Sciences and Engineering Programme, National University of Singapore, Singapore, Singapore. <sup>4</sup>Department of Materials Science and Engineering, National University of Singapore, Singapore, Singapore. ✉email: phyqsy@nus.edu.sg

abelian anyons in ML WSe<sub>2</sub><sup>35</sup> highlights the potential of creating pseudo-spinors from aligned LLs for topological quantum computing applications<sup>36</sup>.

## RESULTS

### Computational approach

For a many-electron system described by a static mean-field Hamiltonian  $H|n\mathbf{k}\rangle = E_{n\mathbf{k}}|n\mathbf{k}\rangle$ , it has been shown that an out-of-plane magnetic field  $B$  results in the following expression for the LLs at the  $K$  valley<sup>6</sup>:

$$\epsilon_{N,\mathbf{K}} = E_{n\mathbf{K}} + \left(N + \frac{1}{2}\right) \frac{2}{m^*} \mu_B B - g_{n\mathbf{K}}^1 \mu_B B, \quad (1)$$

where  $n$  is the corresponding band index,  $E_{n\mathbf{K}}$  is the mean-field single-particle energy at  $K$ ,  $m^*$  is the valley effective mass,  $\mu_B$  is the Bohr magneton, and  $N = 0, 1, 2, \dots$  is the LL index. The total intrinsic single band  $g$ -factor consists of the orbital and spin contribution,  $g_{n\mathbf{K}}^1 = g_{n\mathbf{K}}^{\text{orb}} - g_s s_{z,n\mathbf{K}}$ , where  $g_s$  is taken to be 2.0 and  $s_{z,n\mathbf{K}}$  is the spin quantum number. The orbital component of the intrinsic  $g$ -factor is  $g_{n\mathbf{K}}^{\text{orb}}$ , defined as  $g_{n\mathbf{K}}^{\text{orb}} \mu_B = m_{n\mathbf{K}}^z$ :

$$\mathbf{m}_{n\mathbf{K}} = -\frac{ie}{2\hbar} \langle \partial_{\mathbf{k}} U_{n\mathbf{k}} | \times [H_{\mathbf{k}} - E_{n\mathbf{k}}] | \partial_{\mathbf{k}} U_{n\mathbf{k}} \rangle_{\mathbf{k}=\mathbf{K}}, \quad (2)$$

where it is assumed that the LLs are within the quadratic region of the band extrema<sup>6</sup>.

The above description does not explicitly account for the energy dependence of the electron self-energy  $\Sigma(E)$ . The change in self-energy as the energy shifts with  $B$  leads to an effective renormalized  $g$ -factor,  $g_{n\mathbf{K}}^*$ , defined as  $(\epsilon'_{N,\mathbf{K}} - \epsilon'_{N,\mathbf{K}'}) = -2g_{n\mathbf{K}}^* \mu_B B$  where

$$\begin{aligned} \epsilon'_{N,\mathbf{K}} &= E_{n\mathbf{K}} + \left(N + \frac{1}{2}\right) \frac{2}{m^*} \mu_B B - g_{n\mathbf{K}}^1 \mu_B B + \Sigma(\epsilon'_{N,\mathbf{K}}) \\ \epsilon'_{N,\mathbf{K}'} &= E_{n\mathbf{K}'} + \left(N + \frac{1}{2}\right) \frac{2}{m^*} \mu_B B + g_{n\mathbf{K}'}^1 \mu_B B + \Sigma(\epsilon'_{N,\mathbf{K}'}). \end{aligned} \quad (3)$$

The effects of the self-energy on the  $g$ -factors in carrier-doped silicon systems have been addressed in part by Janak<sup>23</sup> and Ando<sup>28</sup> using a two-dimensional electron gas (2DEG) model. Janak's work had ignored the formation of LLs, replacing  $\epsilon'_{N,\mathbf{K}}$  with the corresponding quasiparticle (QP) levels in the Bloch states<sup>23</sup>. Despite this simplifying assumption, the approach yielded carrier-density-dependent  $g$ -factors in agreement with experiments<sup>24</sup>. Ando modeled approximately the self-energies for LLs, and predicted that the  $g$ -factors should have an oscillatory dependence on the carrier density<sup>28</sup>. This oscillatory dependence primarily arises from the discrete nature of LL states. It was found that the maximum values of the  $g$ -factors predicted by Ando's approach (corresponding to the maxima in the peaks in the oscillations) agreed well with the experiments<sup>37</sup>. In both approaches, it is deduced that the effect of many-body interactions on the  $g$ -factors depends on the difference in occupations between the spin-up and spin-down bands. In the case of doped TMDs, where the spin and valley degrees of freedom are coupled<sup>4,5</sup>, this difference in occupations corresponds to that between the valley extrema at  $K$  and  $K'$ .

In hole-doped TMDs, the large intrinsic  $g$ -factors<sup>6-8</sup> imply that the valley Zeeman effect provides the major contribution to the difference in occupations between  $K$  and  $K'$ —the effect of discrete LLs on this difference is insignificant compared to that of the Zeeman shift. Given the success of Janak's approach, we proceed to use the Bloch state formalism to quantify the change in  $g$ -factors due to self-energy effects. Thus, following Janak,<sup>23</sup> we define  $g_{n\mathbf{K}}^*$  as

$$(E_{n\mathbf{K}}^{\text{QP},1} - E_{n\mathbf{K}'}^{\text{QP},1}) = -2g_{n\mathbf{K}}^* \mu_B B, \quad (4)$$

where

$$\begin{aligned} E_{n\mathbf{K}}^{\text{QP},1} &= E_{n\mathbf{K}} + \Sigma(E_{n\mathbf{K}}^{\text{QP},1}) - g_{n\mathbf{K}}^1 \mu_B B \\ E_{n\mathbf{K}'}^{\text{QP},1} &= E_{n\mathbf{K}'} + \Sigma(E_{n\mathbf{K}'}^{\text{QP},1}) + g_{n\mathbf{K}'}^1 \mu_B B, \end{aligned} \quad (5)$$

and obtain

$$E_{n\mathbf{K}}^{\text{QP},1} - E_{n\mathbf{K}'}^{\text{QP},1} = \Sigma(E_{n\mathbf{K}}^{\text{QP},1}) - \Sigma(E_{n\mathbf{K}'}^{\text{QP},1}) - 2g_{n\mathbf{K}}^1 \mu_B B. \quad (6)$$

As the change in energy ( $E_{n\mathbf{K}}^{\text{QP},1} - E_{n\mathbf{K}'}^{\text{QP},1}$ ) is of the order of meV for typical Zeeman shifts such as those reported here, we can further linearize the change in self-energy using its derivative with respect to the energy argument:

$$\Sigma(E_{n\mathbf{K}}^{\text{QP},1}) - \Sigma(E_{n\mathbf{K}'}^{\text{QP},1}) = \frac{d\Sigma(E)}{dE} (E_{n\mathbf{K}}^{\text{QP},1} - E_{n\mathbf{K}'}^{\text{QP},1}) \quad (7)$$

and

$$\frac{g_{n\mathbf{K}}^1}{g_{n\mathbf{K}}^*} = 1 - \frac{d\Sigma(E)}{dE}. \quad (8)$$

Such a renormalization effect is missing in previous first-principles calculations of  $g$ -factors in TMDs<sup>6-8</sup>.

The electron self-energy in this work is computed within the  $GW$  approximation<sup>38</sup> (see Methods), which uses the first-order term in the perturbative expansion of  $\Sigma$  in terms of the screened Coulomb interaction  $W$ . For undoped systems,  $\frac{d\Sigma(E)}{dE}$  arises from the explicit energy-dependence of  $\Sigma$ , which can be deduced from the ab initio  $GW$  calculation. In contrast to the undoped system, doped systems have partially occupied bands. Thus, if the band occupancies are also changing in response to the magnetic field, there is an additional term in  $\frac{d\Sigma(E)}{dE}$ :

$$\frac{d\Sigma(E)}{dE} = \frac{\partial \Sigma(E)}{\partial E} + \frac{\partial \Sigma(E)}{\partial f} \frac{\partial f}{\partial E}, \quad (9)$$

where  $f$  is the Fermi-Dirac distribution function. The second term in Eq (9) can be simplified to give (see Methods):

$$\frac{\partial \Sigma(E)}{\partial f} \frac{\partial f}{\partial E} \approx \frac{|m^*|}{2\pi} \bar{W}_{nk_f}(E = E_F), \quad (10)$$

where  $n$  is the band index of the frontier doped band, and  $E_F$  and  $k_f$  are respectively the Fermi energy and Fermi wave vector. This term comes from the screened-exchange contribution to self-energy.  $\bar{W}_{nk_f}$  (defined in Methods) is an effective quasi-2D screened Coulomb potential, which can be evaluated completely from the first principles. Since  $\bar{W}_{nk_f}$  is positive, the second term of Eq. (9) leads to an enhancement effect for the  $g$ -factor.

For an ideal 2D fermion gas, the second term of Eq. (9) reduces to the term  $d\Sigma(E)/dE$  derived by Janak in ref. <sup>23</sup> (see also ref. <sup>39</sup> and Supplementary Note). We note that the first term in Eq. (9) is ignored in ref. <sup>23</sup>. Also, in contrast to previous studies<sup>23,28</sup>, we evaluate the screened Coulomb potential from the first principles.

In this work, we limit our considerations to doping densities small enough that the Bloch states involved are within the quadratic region of the valley extrema, so that Eq. (2) holds.

### Renormalized $g$ -factors in undoped TMDs

Table 1 shows the renormalized and intrinsic  $g$ -factors computed for undoped monolayer WSe<sub>2</sub>, using the  $GW$  Hamiltonian. We see that the magnitudes of the renormalized  $g$ -factors are reduced by ~20% compared to the intrinsic  $GW$   $g$ -factors, because  $\frac{\partial \Sigma(E)}{\partial E}$  is in general negative<sup>40</sup>. The exciton  $g$ -factors deduced using the renormalized  $g$ -factors are in good agreement with experiment<sup>41-45</sup>. As discussed in ref. <sup>6</sup>, because the  $X0$  and  $D0$  excitons involve optical transitions in a small region of the Brillouin Zone around  $K$ , the reorganization of Bloch states into LLs does not shift the exciton energies on average.

### Interaction-enhanced g-factors in doped TMDs

We compute the g-factors for hole-doped ML WSe<sub>2</sub> for the valence band at *K*. Henceforth, the subscript *vK* is omitted. The magnitudes of our computed valence band g-factors  $|g^*|$  are plotted as red squares in Fig. 1b for ML WSe<sub>2</sub> with different hole densities. Our predicted g-factors agree well with those deduced from multiple experiments<sup>10,14,16,18</sup> on hole-doped ML WSe<sub>2</sub>. The renormalized g-factor for the undoped system is labeled  $g_0^*$ . Due to interaction-induced enhancement, the g-factor increases significantly once hole carriers are introduced. This enhancement reduces as the hole density is increased as expected from the density dependence of the many-body Coulomb interactions (see Supplementary Fig. 1).

We note that our numerical results for the screened Coulomb potential,  $\bar{W}_{vK_F}$  (see Eq. (12)) differ from those computed for an ideal 2DEG<sup>23,46</sup>, although the corresponding numerical results for the bare Coulomb potential match well with the ideal 2D case (see Supplementary Fig. 1b). This observation implies that an ab initio non-local description of the dielectric function of the quasi-2D system is important for a quantitative prediction of the renormalized g-factors. In both the ab initio and 2DEG approaches, an increase in spin degeneracy reduces  $\bar{W}_{vK_F}$  (see Supplementary Fig. 1a). Thus, the large spin-orbit splitting of ~400 meV in the valence band of ML WSe<sub>2</sub> is an important

	Renormalized ( $g^*$ )	Intrinsic ( $g$ )
$g_{c\uparrow}$	-4.36	-5.50
$g_{c\downarrow}$	-2.05	-2.59
$g_{v\uparrow}$	-6.63	-8.31
$g_{v\downarrow}$	-4.48	-5.62
$g_{X0}$	-4.54	
Expt.	-3.7 <sup>41,42</sup> -4.3 <sup>44</sup> -4.37 <sup>43</sup> -4.4 <sup>45</sup>	
$g_{D0}$	-9.16	
Expt.	-9.3 <sup>42</sup> -9.5 <sup>45</sup> -9.9 <sup>54</sup>	

*c* and *v* refer to the frontier conduction and valence bands, respectively, while  $\uparrow$  and  $\downarrow$  refer to spin up and spin down bands at *K*. *X0* and *D0* refer to the lowest energy spin-allowed and spin-forbidden optical transitions. The exciton g-factors are defined by  $g_{X0} = 2(g_{v\uparrow} - g_{c\uparrow})$  and  $g_{D0} = 2(g_{v\downarrow} - g_{c\downarrow})$ .

underlying reason for the huge g-factor enhancement observed in experiment<sup>10,14,16,18</sup>.

We also plot in Supplementary Fig. 2 the renormalized g-factors when the explicit energy-dependence of the self-energy is ignored. The results show that the explicit energy-dependence of the self-energy reduces the predicted  $|g^*|$  values, resulting in better agreement with the experiment.

### Critical magnetic field

A subtle but important point is that Eq. (10) applies only when the band occupancies are changing with *B*, and the Fermi level  $E_F$  is fixed. In electrostatic gating experiments, the carrier concentration is fixed rather than the absolute Fermi level. However, the Zeeman shifts in *K* and *K'* are equal in magnitude but opposite in sign (Fig. 2a,  $B < B_c$ ), and the density of states for the quadratic bands in 2D is independent of energy. So for *B* small enough that both valleys have carriers (mixed-polarized regime; Fig. 1a),  $E_F$  is fixed while the band occupancies change and both terms in Eq. (9) will apply, leading to the interaction-enhanced g-factors, which we label as  $g_{\text{enh}}^*$ . However, above a critical magnetic field  $B_c \sim |E_F|/(|g_{\text{enh}}^*|\mu_B)$ , only one valley has carriers (Fig. 2a,  $B > B_c$ ) (see Supplementary Note for a more precise expression for  $B_c$ ). As *B* increases beyond  $B_c$ , a constant hole density is maintained when  $E_F$  shifts with the bands without changing the band occupancies. Thus, for  $B > B_c$ , only the first term in Eq. (9) applies, similar to the undoped case, leading to an abrupt drop in  $g^*$  at  $B = B_c$  (Fig. 2b), with a corresponding piecewise-linear Zeeman split  $E_Z$  (Fig. 2c) (see Methods). For a hole density of  $2.5 \times 10^{12} \text{ cm}^{-2}$ ,  $B_c \approx 17 \text{ T}$ , and we have  $g^* \approx -12.2$  for  $B < B_c$  and  $g^* \approx -6.6$  for  $B > B_c$ .

This abrupt drop in  $g^*$  at a critical magnetic field has never been reported or predicted before in traditional valleytronic materials such as silicon. Indeed,  $B_c$  is inversely related to  $|g_{\text{enh}}^*|$ , and it is the large intrinsic g-factors and hence large renormalized g-factors for TMDs that allow for  $B_c$  to be small enough to be reached in standard laboratories. For the same hole density of  $2.5 \times 10^{12} \text{ cm}^{-2}$ , we predict  $B_c$  in silicon to be ~200 T. The larger intrinsic g-factors for TMD MLs arise from the large orbital g-factors, which consist of a valley term, an orbital term, and a cross term that involves coupling between the phase-winding of the Bloch states and the parent atomic orbitals.<sup>6</sup>

Since  $B_c$  is the value of *B* characterizing the onset of the fully-polarized regime,  $B_c$  can be deduced using optical measurements of the exciton and polaron energies for *K* and *K'*<sup>16</sup>. In Fig. 3a, we plot these values of  $B_c$  (blue circles) and compare them with our predicted values (red squares). The predicted dependence of  $B_c$  on

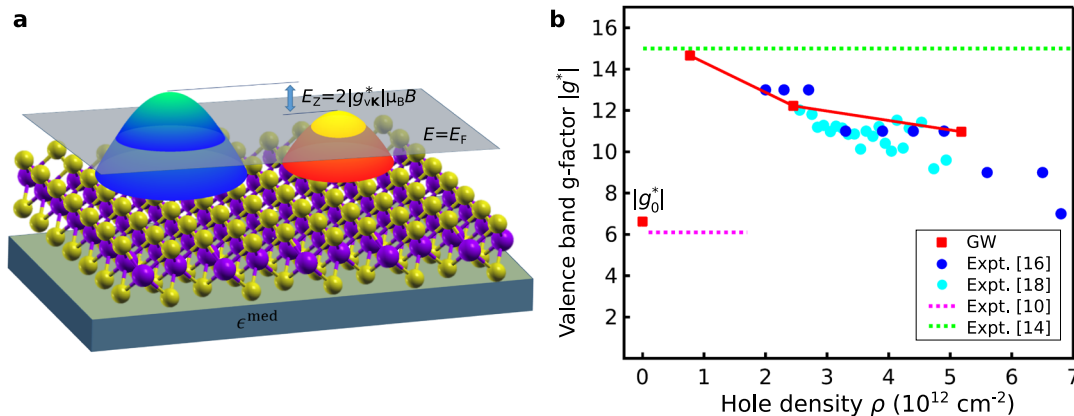


**Fig. 1** Valence band g-factor in hole-doped ML WSe<sub>2</sub>. **a** Schematic figure of the energy dispersion of hole-doped WSe<sub>2</sub> ML in the presence of an out-of-plane magnetic field, in the mixed-polarized regime where the g-factor is enhanced. **b** Valence band g-factor  $|g^*|$  in hole-doped ML WSe<sub>2</sub> as a function of hole density. Red squares: Calculated results; Dark blue and light blue circles: Experimental data from refs. <sup>16,18</sup>, respectively; Purple and green dotted lines: Experimental data from refs. <sup>10,14</sup>, respectively (hole densities are given in a range only).

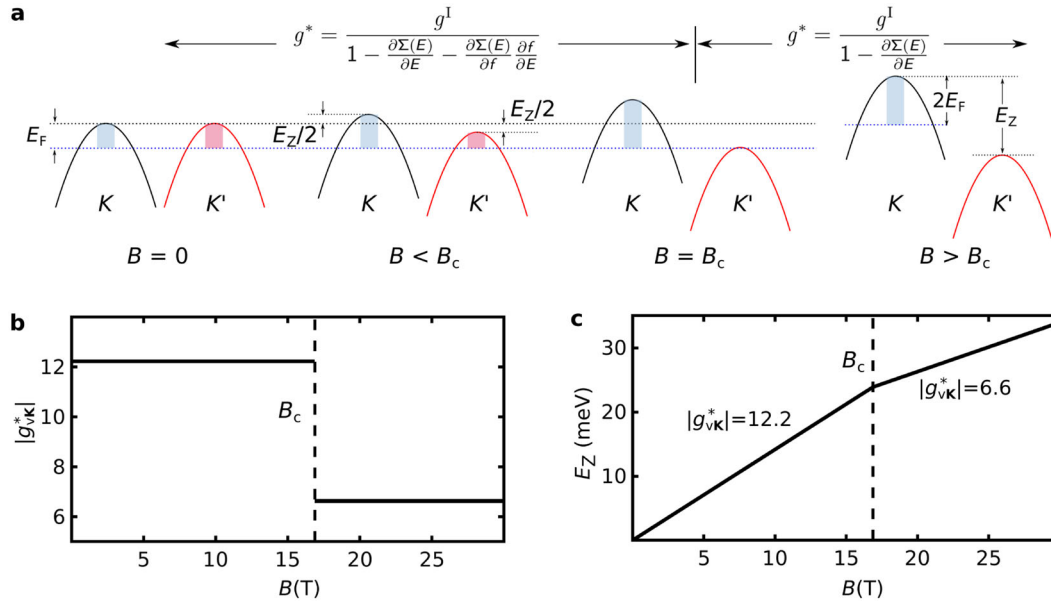


**Fig. 2 Magnetic field dependence of g-factor.** **a** Schematic figure illustrating the Zeeman effect as  $B$  is increased with fixed hole density. The black and red curves represent spin-up and spin-down bands, respectively. The pink and blue shaded regions illustrate the magnitude of hole density due to the constant density of states in the quadratic band in two dimensions. As  $B$  increases for  $B \leq B_c$ , the absolute Fermi level position is unchanged, but the band occupancies change. For  $B > B_c$ , the Fermi level shifts with the band at  $K$  and the band occupancies remain unchanged. **b, c** Plots of **b**  $|g^*_{vK}|$  and **c** valley Zeeman split  $E_Z$  (labeled in **a**) as a function of magnetic field  $B$  for monolayer  $\text{WSe}_2$  with hole density  $2.5 \times 10^{12} \text{ cm}^{-2}$ , which corresponds to  $E_F = 12.2 \text{ meV}$  (see panel **a** for the definition of  $E_F$ ).

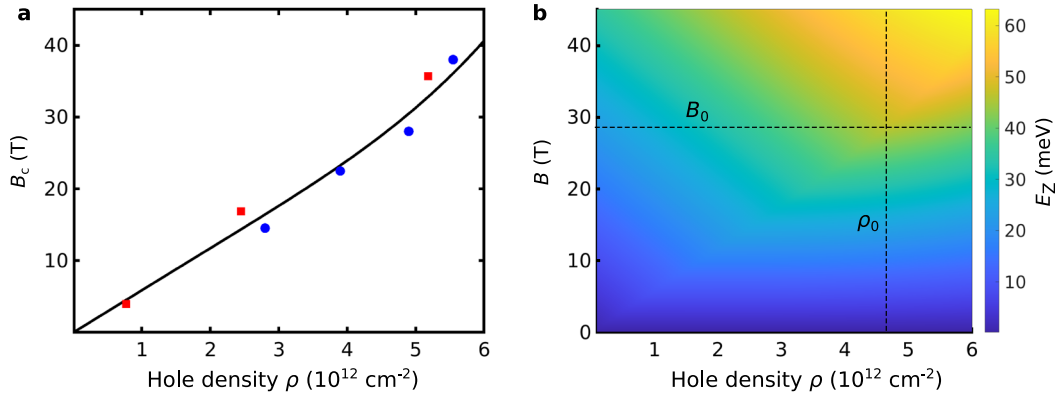


**Fig. 3 Critical magnetic field and Zeeman split.** **a** Critical magnetic field as a function of hole density. Blue circles: experiment<sup>16</sup>; Red squares: our predictions **(b)** 2D plot for  $E_Z$  as a function of hole density and external magnetic field. This plot ignores valley-filling instability effects discussed in Fig. 4.

the hole density agrees well with the experiment. Noting that the definition of  $B_c$  as the onset of the fully-polarized regime can be unambiguously determined in the experiment, the good agreement with the experiment provides further evidence of the accuracy of our predicted carrier-density-dependent g-factors.

How can one maximize the concentration of valley-(and spin-) polarized carriers in the TMD ML? As the hole concentration increases,  $B_c$  increases, giving a larger range of  $B$  for which  $g^*$  is enhanced by interactions (Fig. 3a). However, the magnitude of  $g^*_{\text{enh}}$  decreases as the hole concentration increases (Fig. 1). These competing effects imply that for any given  $B$  field  $B_0$ , there is an optimal hole concentration  $\rho_0$  which maximizes the Zeeman split  $E_Z$  (Fig. 3b). This optimal hole concentration  $\rho_0$  corresponds to the hole concentration for which  $B_c = B_0$  (Fig. 3), and yields a maximum concentration of valley-polarized carriers. These predictions are useful for realizations of the valley Hall effect and other applications where a high concentration of valley-polarized carriers is desired.

### LL alignment and valley-filling instability

The abrupt change in  $g^*$  at  $B = B_c$  also has other interesting implications. We denote the  $N$ th LL at  $K$  as “( $N, K$ )”. As  $B$  increases beyond  $B_c$ , the decrease in  $|g^*|$  results in a decrease in the magnitude of the slopes of the LL fan diagrams (Fig. 4a), leading to a crossing between the energies of ( $0, K'$ ) and ( $N, K$ ) for some  $N$  (purple circle,  $N = 5$  in Fig. 4a) at  $B = B_x$ . If this LL ( $N, K$ ) has carriers, such a LL alignment results in a valley-filling instability, where the hole population is transferred back and forth between the two valleys for small changes in  $B$ .

In Fig. 4b, the blue and pink shading indicate schematically the filling of the LLs with holes, for a constant hole density. As the LL degeneracy is proportional to the LL spacing, when ( $N, K$ ) is fully occupied, we shade the area from  $\epsilon_{N,K} + \frac{\hbar\omega_c}{2}$  down to  $\epsilon_{N,K} - \frac{\hbar\omega_c}{2}$  (blue for  $K$  and pink for  $K'$ ), where the cyclotron frequency  $\omega_c$  is given by  $\omega_c = eB/m^*$ . When a LL ( $\epsilon_{N,K}$ ) is partially filled, the corresponding portion starting from  $\epsilon_{N,K} + \frac{\hbar\omega_c}{2}$  is shaded. In Fig. 4c, the same blue and pink colors are used to represent the total hole

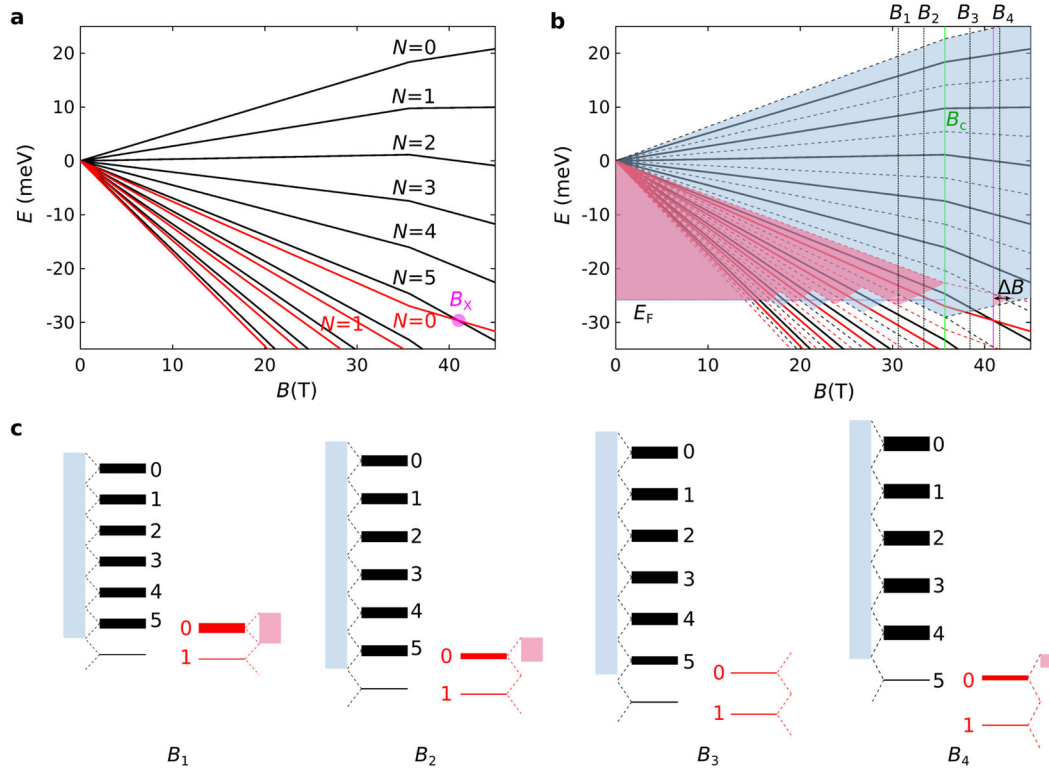


**Fig. 4 LL fan diagram and valley-filling instability.** **a** LL fan diagram for ML WSe<sub>2</sub> valence band with a hole density of  $5.2 \times 10^{12} \text{ cm}^{-2}$  ( $E_F = 25.8 \text{ meV}$ ). The LLs are labeled by the LL index  $N$  and black/red lines and labels represent LLs in valley  $K/K'$ . The slopes of the plots decrease in magnitude when  $B$  increases beyond  $B_c$ , leading to a crossing between  $(0, K')$  and  $(5, K)$  (purple circle). **b** Hole occupancies of LLs in valley  $K/K'$  denoted by blue/pink shading. If the  $N$ th LL at  $K$  is fully occupied with holes for  $(B, B + \delta B)$ , the region  $(\epsilon_{N,K} - \frac{\hbar\omega_c}{2}, \epsilon_{N,K} + \frac{\hbar\omega_c}{2})$  is shaded for  $(B, B + \delta B)$ . Dashed fan diagram lines indicate  $\epsilon_{N,K} \pm \frac{\hbar\omega_c}{2}$ . Holes preferentially occupy LLs with higher energies, and each LL is fully occupied before the next LL lower in energy, resulting in the zigzag fine-structure at  $E \sim E_F$ . **c** Schematic figure for LLs at  $B_1, B_2, B_3$ , and  $B_4$  as marked in **(b)**. The blue and pink shading represent the hole populations in  $K$  and  $K'$ , respectively. The thickness of the black and red lines representing the LLs indicates the hole occupancies of individual LLs in  $K$  and  $K'$ , respectively (a thicker line carries more holes, and the thinnest lines have no holes at all).

occupancy in each valley, at specific values of  $B$ . The hole occupancy of individual LLs is further indicated by the thickness of the black (for  $K$ ) and red (for  $K'$ ) lines representing the LLs. Holes preferentially occupy LLs with higher energies, and each LL is fully occupied before the next LL lower in energy, resulting in a symmetric zigzag fine structure about the original Fermi level  $E_F$ . We note that the large  $g$ -factors in ML WSe<sub>2</sub> imply that this fine structure does not have a significant impact on the difference in hole occupancies between  $K$  and  $K'$ , which is dominated by the Zeeman shifts of the Bloch states. For the purposes of illustration, we see that at  $B_1$  (Fig. 4b, c), the LLs from  $N=0$  to  $N=5$  at  $K$ , and  $(0, K')$  are fully occupied with holes, and all other LLs have no holes. For  $B_2 > B_1$ , the LL degeneracy increases and  $(0, K')$  becomes partially occupied because the  $N=0$  to  $N=5$  LLs at  $K$  can hold more holes, and are all higher in energy than  $(0, K')$ . As  $B$  increases slightly above  $B_c$ , at  $B_3$ , only the  $K$  valley is filled with holes. However, at  $B_4$ , a magnetic field slightly larger than the purple crossing point marked in Fig. 4a, b ( $B_x$ ), holes start to fill the  $K'$  valley again because  $(0, K')$  is higher in energy than  $(5, K)$ . This represents a valley-filling instability, where  $K'$  is depleted of holes from  $B = B_c$  to  $B = B_x$ , and filled again up to  $B_x + \Delta B$  (see Fig. 4b and Supplementary Fig. 3b), when the  $B$  field is large enough that the  $N=0$  to  $N=4$  LLs at  $K$  can contain all the holes and the system becomes fully polarized again. In practice, when holes begin to fill  $(0, K')$ , the mixed-polarized regime is reached and  $g^*$  becomes enhanced, leading to a change in the slope of the fan diagram that is expected to result in a LL alignment not just for  $B = B_x$  but also for  $B$  up to  $B_x + \Delta B$ .

Our predictions provide important theoretical insights into a recent experiment on doped ML WSe<sub>2</sub><sup>16</sup>, where optical absorption plots showed a pronounced signature of the peak positions changing from one inter-LL transition to another over a small range of  $B$  close to the onset of the fully-polarized regime in the experiment. This is consistent with the highest occupied LL in the  $K'$  valley being emptied and partially filled with holes at  $B \sim B_c$  in our predictions. The authors of ref.<sup>16</sup> attributed this observation to the oscillatory  $g$ -factors predicted by Ando for silicon<sup>28</sup>. However, in this theory, the changes in the  $g$ -factors are directly related to the position of the Fermi level relative to the LLs, and the  $g$ -factors, therefore, have an “oscillatory”<sup>28</sup> dependence on  $B$  rather than a pronounced change at one particular value of  $B$  as seen in the experiment. Furthermore, such a pronounced instability was not observed in experiments<sup>24–27</sup> on the  $g$ -factors in doped silicon and other traditional valleytronic materials for which these oscillatory  $g$ -factors were predicted. Thus, this pronounced instability observed in doped ML WSe<sub>2</sub><sup>16</sup> is in fact a manifestation of the valley-filling instabilities that are predicted here to emerge specifically for doped TMDs. Our conclusion is further supported by the fact that the measured values of  $B_c$  and  $B_x$  are respectively 32 and 38 T for  $|g_{\text{enh}}^*| \sim 11$ <sup>16</sup>, close to our predicted values of 31 and 37 T for the same  $|g_{\text{enh}}^*|$  (see also Supplementary Table 1).

The alignment of LLs is of interest to investigate quantum phase transitions in these doped TMDs<sup>16,29–34</sup>. Given that the LLs are expected to align for  $B$  between  $B_x$  and  $B_x + \Delta B$ , it is interesting to predict how large  $\Delta B$  can be and how sensitive  $\Delta B$  is to

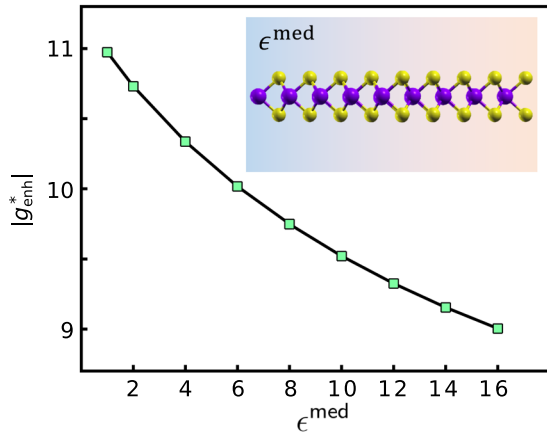


**Fig. 5 Tunability of  $|g_{\text{enh}}^*|$  using dielectric screening.** Ab initio valence band g-factor  $|g_{\text{enh}}^*|$  as a function of background dielectric constant  $\epsilon^{\text{med}}$  for a hole density of  $5.18 \times 10^{12} \text{ cm}^{-2}$ .

fluctuations in  $g_{\text{enh}}^*$ . Not all values of  $g_{\text{enh}}^*$  will result in instability (see Supplementary Fig. 3a and Supplementary Note). In particular, if the energies of  $(0, K')$  and  $(N, K)$  cross at  $B_x$ , the valley-filling instability only occurs if  $(N, K)$  is occupied with holes. Supplementary Fig. 3c plots the ranges of  $g_{\text{enh}}^*$  for which a valley-filling instability will occur, as well as the corresponding  $\Delta B$  values. We see that an optimal range of  $|g_{\text{enh}}^*|$  for LL alignment is  $10.4 < |g_{\text{enh}}^*| < 11.2$ . Here,  $\Delta B$  is quite large ( $\sim 8$  T for  $|g_{\text{enh}}^*| \sim 10.4$ ) and is also fairly robust to changes in  $g_{\text{enh}}^*$ . The corresponding values of  $B_c$  and  $B_x$  fall within 30 to 40 T (Supplementary Table 1), well within the reach of experiments.

The alignment of LLs in different valleys can in principle be achieved for  $B < B_c$  if  $g_{\text{enh}}^*$  can be tuned such that  $(0, K')$  matches exactly with  $(N, K)$  for some  $N$ . However, once  $g_{\text{enh}}^*$  deviates slightly from this value, due to fluctuations in the hole density or dielectric environment (see Fig. 5), the LLs are no longer aligned. Our predictions above enable the alignment of LLs while allowing for some fluctuations in  $g_{\text{enh}}^*$ .

### Tunability of interaction-enhanced g-factor

We further note that in addition to electrostatic gating which changes the carrier concentration and thus  $g_{\text{enh}}^*$  (Fig. 1),  $g_{\text{enh}}^*$  can also be tuned by dielectric screening (Fig. 5). The tunability of  $g_{\text{enh}}^*$  with the background dielectric constant can be understood from the fact that  $g_{\text{enh}}^*$  is related to the effective quasi-2D screened Coulomb potential at the Fermi surface (Eq. (10)). This tunability of  $g_{\text{enh}}^*$  provides a handle to control the valley-polarized current,  $B_c$  and  $\Delta B$ . We note that in ref. 16, the substrate for ML WSe<sub>2</sub> is hexagonal boron nitride (hBN), which has a large band gap and minimal impact on the computed g-factors (see Supplementary Fig. 1a). On the other hand, we predict that layered MoSe<sub>2</sub>, which corresponds to  $\epsilon^{\text{med}} \sim 9$ , can reduce  $g_{\text{enh}}^*$  by more than 10%.

### DISCUSSION

In summary, our ab initio calculations show that many-body interactions in doped TMD MLs enhance the g-factors compared to the undoped MLs, up to a critical magnetic field  $B_c$  above which the g-factors revert to those in the undoped systems. Such a phenomenon has not been predicted or observed in silicon and other traditional valleytronic materials, because the corresponding  $B_c$  would be much larger due to the smaller g-factors in these materials.

The enhancement in g-factors arises from the effect of a magnetic-field-induced change in occupancies on the screened-exchange interactions. This effect is only present in the mixed-

polarized regime ( $B < B_c$ ). As the carrier concentration increases,  $g^*$  decreases and  $B_c$  increases, so that for any value of the magnetic field  $B_0$ , the valley-polarization is maximized when the carrier concentration is such that  $B_c = B_0$ . This prediction has implications for maximizing the valley- and spin-polarized current for the valley Hall effect.

The computed interaction-enhanced g-factors agree well with experiments for different doping concentrations. Both the explicit dependence of the self-energy on energy and the effects of changes in occupancies are required to obtain good agreement with the experiment. The crucial energy dependence of the self-energy implies that standard Kohn–Sham density functional theory (DFT) cannot be used to predict the Landé g-factors of doped systems. However, doping-dependent exchange-correlation functionals that can accurately describe the dependence of the self-energy on occupancies may capture the enhancement effect due to changes in occupancies.

We further identify the values of  $g_{\text{enh}}^*$  and corresponding ranges of  $B$  that lead to a valley-filling instability and expected LL alignment, which are of interest for the investigation of quantum phase transitions in doped TMDs<sup>29–34</sup>. Recent observations of fractional quantum Hall states associated with non-abelian anyons in ML WSe<sub>2</sub><sup>35</sup> suggest that the creation of pseudo-spinors from a linear combination of valley-aligned LLs can be useful for topological quantum computing applications<sup>36</sup>.

### METHODS

#### Intrinsic g-factor

To compute the intrinsic g-factors, we use the PBE exchange-correlation functional<sup>47</sup> for the DFT mean-field calculations<sup>48</sup> and the details follow those in ref. 6. For GW calculations of the intrinsic g-factors, we use a non-uniform sampling method<sup>49</sup> of the Brillouin Zone starting with a  $12 \times 12$  k-grid as implemented in the BerkeleyGW code<sup>50</sup>. The energy dependence of the dielectric function is treated within the generalized plasmon pole (GPP) model<sup>40</sup>. An energy cutoff of 35 Ry with 4000 empty bands is used for the reciprocal space expansion of the static dielectric matrix, which is computed within the random phase approximation. The intrinsic single band g-factor reduces by only 0.2 when an energy cutoff of 2Ry with 200 empty bands is used.

#### Renormalized g-factor for $B < B_c$

The renormalized g-factor  $g^*$  is computed from the intrinsic g-factor  $g^l$  and  $\frac{d\Sigma(E)}{dE}$  using Eq. (8). We approximate  $g^l$  using the value in the undoped system. The intrinsic single band g-factors from DFT calculations do not change when ML WSe<sub>2</sub> is doped with holes.

The first term of Eq. (9) can be obtained directly from the BerkeleyGW output<sup>50</sup>.

$\Sigma = i\text{GW}$  can be partitioned<sup>40</sup> into the dynamical non-local screened-exchange (SEX) and Coulomb-hole (COH) interaction terms  $\Sigma = \Sigma^{\text{SEX}} + \Sigma^{\text{COH}}$ . Only the screened-exchange term depends on the occupancies  $f$  and contributes to the second term of Eq. (9). The screened-exchange energy  $\Sigma^{\text{SEX}}$  in our ab initio plane-wave calculation can be written as (see Supplemental Note):

$$\begin{aligned} \Sigma_{n\mathbf{K}}^{\text{SEX}}(E) &= - \sum_m \frac{1}{N_q \Omega} \sum_{\mathbf{q}\mathbf{G}\mathbf{G}'} f_{m\mathbf{K}-\mathbf{q}} \langle n\mathbf{K} | e^{i(\mathbf{q}+\mathbf{G})\cdot\mathbf{r}} | m\mathbf{K}-\mathbf{q} \rangle \langle m\mathbf{K}-\mathbf{q} | e^{-i(\mathbf{q}+\mathbf{G}')\cdot\mathbf{r}} | n\mathbf{K} \rangle \\ &\quad \times \epsilon_{\mathbf{G}\mathbf{G}'}^{-1}(\mathbf{q}, E - E_{m\mathbf{K}-\mathbf{q}}) v_{\mathbf{q}+\mathbf{G}} \\ &= - \sum_m \frac{1}{(2\pi)^2} \int_{BZ} d^2q \bar{W}_{m\mathbf{q}} f_{m\mathbf{K}-\mathbf{q}}, \end{aligned} \quad (11)$$

where we define the quasi-2D screened Coulomb potential:

$$\begin{aligned} \bar{W}_{m\mathbf{q}}(E) &= \frac{1}{L} \sum_{\mathbf{G}\mathbf{G}'} \langle n\mathbf{K} | e^{i(\mathbf{q}+\mathbf{G})\cdot\mathbf{r}} | m\mathbf{K}-\mathbf{q} \rangle \langle m\mathbf{K}-\mathbf{q} | e^{-i(\mathbf{q}+\mathbf{G}')\cdot\mathbf{r}} | n\mathbf{K} \rangle \\ &\quad \times \epsilon_{\mathbf{G}\mathbf{G}'}^{-1}(\mathbf{q}, E - E_{m\mathbf{K}-\mathbf{q}}) v_{\mathbf{q}+\mathbf{G}}. \end{aligned} \quad (12)$$

Here,  $\Omega$  is the cell volume,  $N_q$  is the number of q-points, and  $v_{\mathbf{q}}$  is the Coulomb potential with the slab Coulomb truncation scheme applied<sup>51</sup>.  $\bar{W}_{m\mathbf{q}}$  is an effective quasi-2D screened Coulomb potential defined in valley  $K$  and  $L$  is the height of the supercell for ML WSe<sub>2</sub>. The non-local nature of the dielectric matrix is fully taken into account in  $\epsilon_{\mathbf{G}\mathbf{G}'}^{-1}(\mathbf{q}, E - E_{m\mathbf{K}-\mathbf{q}})$ . The

second term in Eq. (9) is then given by (see Supplemental Note):

$$\frac{\partial \Sigma(E)}{\partial E} \frac{\partial f}{\partial E} = - \sum_m \frac{1}{(2\pi)^2} \int_{BZ} d^2 q \overline{W}_{m\mathbf{q}} \frac{\partial f_{m\mathbf{k}-\mathbf{q}}}{\partial E} \approx \frac{|m^*|}{2\pi} \overline{W}_{nk_f}(E = E_F). \quad (13)$$

Here, we have neglected the contribution of intervalley scattering to the self-energy. Our calculations show that the intervalley contributions to the plane-wave matrix elements  $\{\langle n\mathbf{K}|e^{i(\mathbf{q}+\mathbf{G})\cdot\mathbf{r}}|m\mathbf{K}-\mathbf{q}\rangle\}$  are an order of magnitude smaller than the intravalley ones. We compute  $g_{\mathbf{v}\mathbf{k}}^*$  by evaluating  $\overline{W}_{vk_f}$  ab initio using the random phase approximation for the dielectric matrix. Due to the partial occupancies, we calculate the dielectric matrix using a dense reciprocal space sampling of  $120 \times 120$ , a 2Ry  $G$ -vector cut off and 29 bands.  $g^*$  is unchanged when we use instead 4Ry and 299 bands, and reduces by  $\sim 3\%$  when a  $240 \times 240$  k-mesh is used. Care is taken to include the effect of spin-orbit splitting at the valleys. For the effective mass, we use our DFT value of  $m^* = -0.48m_e$ , which agrees well with the experimentally deduced value for hole-doped  $\text{WSe}_2$ <sup>52</sup>. If electronic screening is ignored, the effective quasi-2D bare Coulomb potential  $\overline{V}_{mq}$  is defined by:

$$\overline{V}_{mq}(E) = \frac{1}{L} \sum_{\mathbf{G}\mathbf{G}'} \langle n\mathbf{K}|e^{i(\mathbf{q}+\mathbf{G})\cdot\mathbf{r}}|m\mathbf{k}-\mathbf{q}\rangle \langle m\mathbf{k}-\mathbf{q}|e^{-i(\mathbf{q}+\mathbf{G}')\cdot\mathbf{r}}|n\mathbf{K}\rangle \delta_{\mathbf{G}\mathbf{G}'} v_{\mathbf{q}+\mathbf{G}}. \quad (14)$$

Our first-principles results for  $\overline{V}_{vk_f}$  (Supplementary Fig. 1b) agrees with the analytically-derived 2D Coulomb potential. At low doping densities,  $\overline{V}_{vk_f}$  is very large, which would change the sign of  $g^*$  compared to the intrinsic  $g$ -factor, indicating that screening is important for a meaningful description of  $g^*$ .

### Renormalized $g$ -factor for $B > B_c$

For  $B > B_c$ ,  $\frac{d\Sigma(E)}{dE} = \frac{\partial \Sigma(E)}{\partial E}$ . We define  $g_{n\mathbf{K}}^*$  as

$$((E_{n\mathbf{K}}^{\text{QP},2} - E_{n\mathbf{K}}^{\text{QP},1}) - (E_{n\mathbf{K}}^{\text{QP},1} - E_{n\mathbf{K}}^{\text{QP},1})) = -2g_{n\mathbf{K}}^* \mu_B (B_2 - B_1), \quad (15)$$

Equivalently,

$$(E_{n\mathbf{K}}^{\text{QP},2} - E_{n\mathbf{K}}^{\text{QP},1}) = -g_{n\mathbf{K}}^* \mu_B (B_2 - B_1), \quad (16)$$

where

$$\begin{aligned} E_{n\mathbf{K}}^{\text{QP},1} &= E_{n\mathbf{K}} + \Sigma(E_{n\mathbf{K}}^{\text{QP},1}) - g_{n\mathbf{K}}^1 \mu_B B_1 \\ E_{n\mathbf{K}}^{\text{QP},2} &= E_{n\mathbf{K}} + \Sigma(E_{n\mathbf{K}}^{\text{QP},2}) - g_{n\mathbf{K}}^1 \mu_B B_2, \end{aligned} \quad (17)$$

so that

$$E_{n\mathbf{K}}^{\text{QP},2} - E_{n\mathbf{K}}^{\text{QP},1} = \Sigma(E_{n\mathbf{K}}^{\text{QP},2}) - \Sigma(E_{n\mathbf{K}}^{\text{QP},1}) - g_{n\mathbf{K}}^1 \mu_B (B_2 - B_1). \quad (18)$$

Since

$$\Sigma(E_{n\mathbf{K}}^{\text{QP},2}) - \Sigma(E_{n\mathbf{K}}^{\text{QP},1}) \approx \frac{d\Sigma(E)}{dE} (E_{n\mathbf{K}}^{\text{QP},2} - E_{n\mathbf{K}}^{\text{QP},1}), \quad (19)$$

we obtain

$$\frac{g_{n\mathbf{K}}^1}{g_{n\mathbf{K}}^*} = 1 - \frac{d\Sigma(E)}{dE} = 1 - \frac{\partial \Sigma(E)}{\partial E}. \quad (20)$$

### Background dielectric constant

A uniform background dielectric constant ( $\epsilon^{\text{med}}$ ) can be simply added to the dielectric function of the system to obtain the total dielectric function:  $\epsilon(\mathbf{r}, \mathbf{r}', \omega) = \epsilon^{\text{WSe}_2}(\mathbf{r}, \mathbf{r}', \omega) + \epsilon^{\text{med}} - 1$ . In our first-principles calculation, the dielectric function is expanded in a plane-wave basis:  $\epsilon(\mathbf{r}, \mathbf{r}', \omega) = \sum_{\mathbf{q}\mathbf{G}\mathbf{G}'} e^{i(\mathbf{q}+\mathbf{G})\cdot\mathbf{r}} \epsilon_{\mathbf{G}\mathbf{G}'}(\mathbf{q}, \omega) e^{-i(\mathbf{q}+\mathbf{G}')\cdot\mathbf{r}'}$ . Thus we approximate the effect of screening by a dielectric medium by modifying the static dielectric matrix as follows:

$$\epsilon_{\mathbf{G}\mathbf{G}'}(\mathbf{q}, 0) = \epsilon_{\mathbf{G}\mathbf{G}'}^{\text{WSe}_2} + (\epsilon^{\text{med}} - 1) \delta_{\mathbf{G}\mathbf{G}'}. \quad (21)$$

We approximate the dielectric screening from a substrate using  $\epsilon^{\text{med}} = (1 + \epsilon^{\text{sub}})/2$ <sup>53</sup>, where  $\epsilon^{\text{sub}}$  is the dielectric constant of the substrate.

### DATA AVAILABILITY

The data that support the findings of this study are available from the corresponding author upon reasonable request.

### CODE AVAILABILITY

The QuantumESPRESSO and BerkeleyGW packages used in this work are open sources. The codes for the calculation of Eq. (2) and Eq. (12) are available from the corresponding author upon reasonable request.

Received: 5 May 2021; Accepted: 27 October 2021;

Published online: 09 December 2021

### REFERENCES

- Ohkawa, F. J. & Uemura, Y. Theory of valley splitting in an  $N$  channel (100) inversion layer of Si I. Formulation by extended zone effective mass theory. *J. Phys. Soc. Jpn.* **43**, 907–916 (1977).
- Sham, L. J., Allen Jr, S. J., Kamgar, A. & Tsui, D. C. Valley-valley splitting in inversion layers on a high-index surface of silicon. *Phys. Rev. Lett.* **40**, 472–475 (1978).
- Schaibley, J. R. et al. Valleytronics in 2D materials. *Nat. Rev. Mater.* **1**, 16055 (2016).
- Wang, G. et al. Colloquium: excitons in atomically thin transition metal dichalcogenides. *Rev. Mod. Phys.* **90**, 021001 (2018).
- Xiao, D., Liu, G.-B., Feng, W., Xu, X. & Yao, W. Coupled spin and valley physics in monolayers of  $\text{MoS}_2$  and other group-VI dichalcogenides. *Phys. Rev. Lett.* **108**, 196802 (2012).
- Xuan, F. & Quek, S. Y. Valley Zeeman effect and Landau levels in two-dimensional transition metal dichalcogenides. *Phys. Rev. Res.* **2**, 033256 (2020).
- Deilmann, T., Krüger, P. & M, R. Ab Initio studies of exciton  $g$  factors: monolayer transition metal dichalcogenides in magnetic fields. *Phys. Rev. Lett.* **124**, 226402 (2020).
- Woźniak, T., Faria Junior, P. E., Seifert, G., Chaves, A. & Kunstmann, J. Exciton  $g$  factors of van der Waals heterostructures from first-principles calculations. *Phys. Rev. B* **101**, 235408 (2020).
- Förste, J. et al. Exciton  $g$ -factors in monolayer and bilayer  $\text{WSe}_2$  from experiment and theory. *Nat. Commun.* **11**, 4539 (2020).
- Robert, C. et al. Measurement of conduction and valence bands  $g$ -factors in a transition metal dichalcogenide monolayer. *Phys. Rev. Lett.* **126**, 067403 (2021).
- Pisoni, R. et al. Interactions and magnetotransport through spin-valley coupled Landau levels in monolayer  $\text{MoS}_2$ . *Phys. Rev. Lett.* **121**, 247701 (2018).
- Smoleński, T. et al. Interaction-induced Shubnikov-de Haas oscillations in optical conductivity of monolayer  $\text{MoSe}_2$ . *Phys. Rev. Lett.* **123**, 097403 (2019).
- Wang, Z., Shan, J. & Mak, K. F. Valley- and spin-polarized Landau levels in monolayer  $\text{WSe}_2$ . *Nat. Nanotechnol.* **12**, 144–149 (2017).
- Liu, E. et al. Landau-quantized excitonic absorption and luminescence in a monolayer valley semiconductor. *Phys. Rev. Lett.* **124**, 097401 (2020).
- Wang, Z., Mak, K. F. & Shan, J. Strongly interaction-enhanced valley magnetic response in monolayer  $\text{WSe}_2$ . *Phys. Rev. Lett.* **120**, 066402 (2018).
- Li, J. et al. Spontaneous valley polarization of interacting carriers in a monolayer semiconductor. *Phys. Rev. Lett.* **125**, 147602 (2020).
- Lin, J. et al. Determining interaction enhanced valley susceptibility in spin-valley-locked  $\text{MoS}_2$ . *Nano Lett.* **19**, 1736–1742 (2019).
- Gustafsson, M. V. et al. Ambipolar Landau levels and strong band-selective carrier interactions in monolayer  $\text{WSe}_2$ . *Nat. Mater.* **17**, 411–415 (2018).
- Movva, H. C. P. et al. Density-dependent quantum Hall states and Zeeman splitting in monolayer and bilayer  $\text{WSe}_2$ . *Phys. Rev. Lett.* **118**, 247701 (2017).
- Larentis, S. et al. Large effective mass and interaction-enhanced Zeeman splitting of  $K$ -valley electrons in  $\text{MoSe}_2$ . *Phys. Rev. B* **97**, 201407(R) (2018).
- Roth, L. M.  $g$  factor and donor spin-lattice relaxation for electrons in germanium and silicon. *Phys. Rev.* **118**, 1534–1540 (1960).
- Yafet, Y.  $g$  factors and spin-lattice relaxation of conduction electrons. *Solid State Phys.* **14**, 1–98 (1963).
- Janak, J. F.  $g$  factor of the two-dimensional interacting electron gas. *Phys. Rev.* **178**, 1416–1418 (1969).
- Fang, F. F. & Stiles, P. J. Effects of a tilted magnetic field on a two-dimensional electron gas. *Phys. Rev.* **174**, 823–828 (1968).
- Lakhani, A. A. & Stiles, P. J. Experimental study of oscillatory values of  $g^*$  of a two-dimensional electron gas. *Phys. Rev. Lett.* **31**, 25–28 (1973).
- Nicholas, R. J., Haug, R. J., Klitzing, K. V. & Weimann, G. Exchange enhancement of the spin splitting in a  $\text{GaAs-Ga}_x\text{Al}_{1-x}\text{As}$  heterojunction. *Phys. Rev. B* **37**, 1294–1302 (1988).
- Papadakis, S. J., De Poortere, E. P. & Shayegan, M. Anomalous spin splitting of two-dimensional electrons in an AlAs quantum well. *Phys. Rev. B* **59**, R12743 (1999).
- Ando, T. & Uemura, Y. Theory of oscillatory  $g$  factor in an MOS inversion layer under strong magnetic fields. *J. Phys. Soc. Jpn.* **37**, 1044–1052 (1974).
- Braz, J. E. H., Amorim, B. & Castro, E. V. Valley-polarized magnetic state in hole-doped monolayers of transition-metal dichalcogenides. *Phys. Rev. B* **98**, 161406 (2018).

30. van der Donk, M. & Peeters, F. M. Rich many-body phase diagram of electrons and holes in doped monolayer transition metal dichalcogenides. *Phys. Rev. B* **98**, 115432 (2018).
31. Miserev, D., Klinovaja, J. & Loss, D. Exchange intervalley scattering and magnetic phase diagram of transition metal dichalcogenide monolayers. *Phys. Rev. B* **100**, 014428 (2019).
32. Roch, J. G. et al. First-order magnetic phase transition of mobile electrons in monolayer MoS<sub>2</sub>. *Phys. Rev. Lett.* **124**, 187602 (2020).
33. Piazza, V. et al. First-order phase transitions in a quantum Hall ferromagnet. *Nature* **402**, 638–641 (1999).
34. De Poortere, E. P., Tutuc, E., Papadakis, S. J. & Shayegan, M. Resistance spikes at transitions between quantum Hall ferromagnets. *Science* **290**, 1546–1549 (2000).
35. Shi, Q. et al. Odd- and even-denominator fractional quantum Hall states in monolayer WSe<sub>2</sub>. *Nat. Nanotechnol.* **15**, 569–573 (2020).
36. Nayak, C., Simon, S. H., Stern, A., Freedman, M. & Das Sarma, S. Non-Abelian anyons and topological quantum computation. *Rev. Mod. Phys.* **80**, 1083 (2008).
37. Kobayashi, M. & Komatsubara, K. F. On the experimental *g* factor of conduction electrons in n-type inversion layer on silicon (100) surface. *Jpn. J. Appl. Phys.* **2**, 343–346 (1974).
38. Hedin, L. New method for calculating the one-particle green's function with application to the electron-gas problem. *Phys. Rev.* **139**, A796 (1965).
39. Ting, C. S., Lee, T. K. & Quinn, J. J. Effective mass and *g* factor of interacting electrons in the surface inversion layer of silicon. *Phys. Rev. Lett.* **34**, 870–874 (1974).
40. Hybertsen, M. S. & Louie, S. G. Electron correlation in semiconductors and insulators: band gaps and quasiparticle energies. *Phys. Rev. B* **34**, 5390–5413 (1986).
41. Wang, G. et al. Magneto-optics in transition metal diselenide monolayers. *2D Mater.* **2**, 034002 (2015).
42. Li, Z. et al. Emerging photoluminescence from the dark-exciton phonon replica in monolayer WSe<sub>2</sub>. *Nat. Commun.* **10**, 2469 (2019).
43. Srivastava, A. et al. Valley Zeeman effect in elementary optical excitations of monolayer WSe<sub>2</sub>. *Nat. Phys.* **11**, 141–147 (2015).
44. Koperski, M. et al. Orbital, spin and valley contributions to Zeeman splitting of excitonic resonances in MoSe<sub>2</sub>, WSe<sub>2</sub> and WS<sub>2</sub> Monolayers. *2D Mater.* **6**, 015001 (2019).
45. Liu, E. et al. Gate tunable dark trions in monolayer WSe<sub>2</sub>. *Phys. Rev. Lett.* **123**, 027401 (2019).
46. Stern, F. Polarizability of a two-dimensional electron gas. *Phys. Rev. Lett.* **18**, 546–548 (1967).
47. Perdew, J. P., Burke, K. & Ernzerhof, M. Generalized gradient approximation made simple. *Phys. Rev. Lett.* **77**, 3865–3868 (1996).
48. Giannozzi, P. et al. QUANTUM ESPRESSO: a modular and open-source software project for quantum simulations of materials. *J. Phys. Condens. Matter* **21**, 395502 (2009).
49. da Jornada, F. H., Qiu, D. Y. & Louie, S. G. Nonuniform sampling schemes of the Brillouin zone for many-electron perturbation-theory calculations in reduced dimensionality. *Phys. Rev. B* **95**, 035109 (2017).
50. Deslippe, J. et al. BerkeleyGW: a massively parallel computer package for the calculation of the quasiparticle and optical properties of materials and nanostructures. *Comput. Phys. Commun.* **183**, 1269–1289 (2012).
51. Ismail-Beigi, S. Truncation of periodic image interactions for confined systems. *Phys. Rev. B* **73**, 233103 (2006).
52. Fallahazad, B. et al. Shubnikov-de Haas oscillations of high-mobility holes in monolayer and bilayer WSe<sub>2</sub>: Landau level degeneracy, effective mass, and negative compressibility. *Phys. Rev. Lett.* **116**, 086601 (2016).
53. Burson, K. M. et al. Direct imaging of charged impurity density in common graphene substrates. *Nano Lett.* **13**, 3576–3580 (2013).
54. Liu, E. et al. Valley-selective chiral phonon replicas of dark excitons and trions in monolayer WSe<sub>2</sub>. *Phys. Rev. Res.* **1**, 032007(R) (2019).

## ACKNOWLEDGEMENTS

This work is supported by the NUS Provost's Office, the Ministry of Education (MOE 2017-T2-2-139), and the National Research Foundation (NRF), Singapore, under the NRF medium-sized center program. Calculations were performed on the computational cluster in the Centre for Advanced 2D Materials and the National Supercomputing Centre, Singapore.

## AUTHOR CONTRIBUTIONS

S.Y.Q. conceived the project, and supervised the research and the formalisms developed. F.X. developed and implemented the formalism and performed the calculations. F.X. and S.Y.Q. discussed the results, analyzed the data, and wrote the manuscript.

## COMPETING INTERESTS

The authors declare no competing interests.

## ADDITIONAL INFORMATION

**Supplementary information** The online version contains supplementary material available at <https://doi.org/10.1038/s41524-021-00665-8>.

**Correspondence** and requests for materials should be addressed to Su Ying Quek.

**Reprints and permission information** is available at <http://www.nature.com/reprints>

**Publisher's note** Springer Nature remains neutral with regard to jurisdictional claims in published maps and institutional affiliations.



**Open Access** This article is licensed under a Creative Commons Attribution 4.0 International License, which permits use, sharing, adaptation, distribution and reproduction in any medium or format, as long as you give appropriate credit to the original author(s) and the source, provide a link to the Creative Commons license, and indicate if changes were made. The images or other third party material in this article are included in the article's Creative Commons license, unless indicated otherwise in a credit line to the material. If material is not included in the article's Creative Commons license and your intended use is not permitted by statutory regulation or exceeds the permitted use, you will need to obtain permission directly from the copyright holder. To view a copy of this license, visit <http://creativecommons.org/licenses/by/4.0/>.

© The Author(s) 2021, corrected publication 2022